

GT2017-63033

## SPH SIMULATION OF AN AIR-ASSISTED ATOMIZER OPERATING AT HIGH PRESSURE: INFLUENCE OF NON-NEWTONIAN EFFECTS

G. Chaussonnet\*, R. Koch, H.-J. Bauer

Institut für Thermische Strömungsmaschinen  
Karlsruher Institut für Technologie (KIT)  
Kaiserstr. 12  
76131 Karlsruhe, Germany

A. Säger, T. Jakobs, T. Kolb

Institut für Technische Chemie  
Karlsruher Institut für Technologie (KIT)  
P.O. Box 3640  
76021 Karlsruhe, Germany

### ABSTRACT

A twin-fluid atomizer configuration is predicted by means of the 2D weakly-compressible Smooth Particle Hydrodynamics (SPH) method and compared to experiments. The setup consists of an axial liquid jet fragmented by a co-flowing high-speed air stream ( $U_g \approx 60$  m/s) in a pressurized atmosphere up to 11 bar (abs.). Two types of liquid are investigated: a viscous Newtonian liquid ( $\mu_l = 200$  mPas) obtained with a glycerol/water mixture and a viscous non-Newtonian liquid ( $\mu_{l,apparent} \approx 150$  mPas) obtained with a carboxymethyl cellulose (CMC) solution. 3D effects are taken into account in the 2D code by introducing (i) a surface tension term, (ii) a cylindrical viscosity operator and (iii) a modified velocity accounting for the divergence of the volume in the radial direction. The numerical results at high pressure show a good qualitative agreement with experiment, i.e. a correct transition of the atomization regimes with regard to the pressure, and similar dynamics and length scales of the generated ligaments. The predicted frequency of the Kelvin-Helmholtz instability needs a correction factor of 2 to be globally well recovered with the Newtonian liquid. The simulation of the non-Newtonian liquid at high pressure shows a similar breakup regime with finer droplets compared to Newtonian liquids while the simulation at atmospheric pressure shows an apparent viscosity similar to the experiment.

### NOMENCLATURE

#### Symbols

D	Diameter
H	Height
M	Momentum flux ratio
U	Bulk velocity
V	Particle volume
W	Kernel
$\mathbf{f}$	Force
$f$	Frequency
$h$	Smoothing length
$p$	Pressure
$r$	Particle position
$u$	Local velocity

#### Greek Symbols

$\Omega$	Sphere of influence
$\gamma$	Polytropic ratio
$\dot{\gamma}$	Shear rate
$\delta$	Dirac delta function
$\delta_{ij}$	Kronecker symbol
$\kappa$	Curvature
$\mu$	Dynamic viscosity
$\nu$	Kinematic viscosity
$\rho$	Density
$\sigma$	Surface tension
$\tau_{cc}$	Time delay from Cross-Correlation

#### Subscripts

e	Entrainment
g	Gas
l	Liquid
rel	Relative

#### Abbreviations

ATMO	Atmospheric test rig
CMC	Carboxymethyl cellulose
GLR	Gas to liquid ratio
KH	Kelvin-Helmholtz
PAT	Pressurized atomization test rig

### INTRODUCTION

In the context of renewable energies, the gasification process shows the advantage of producing a flexible energy-carrier. Prior to this process, it is necessary to turn a very viscous and non-Newtonian liquid into a spray, and the quality of the atom-

\*geoffroy.chaussonnet@kit.edu

ization has a strong influence on the overall efficiency [1]. It is therefore necessary to optimize the spray generation, *i.e.* to optimize the injecting nozzle. Due to extreme operating conditions of pressure and temperature ( $p = 80$  bar and  $T \approx 1500^\circ\text{C}$ ), the instrumentation of the gasifier is strongly limited, canceling any fine tunings of the prototype by means of experiment. The use of numerical simulation is therefore a promising candidate to achieve this task.

In this paper, the 2D numerical simulation of a simplified nozzle supplied with Newtonian and non-Newtonian fluids is compared to experiments [2–4], in terms of primary instability, breakup regime and instability frequency. The employed numerical approach is Smooth Particle Hydrodynamics (SPH). It is a mesh-free method that relies on a Lagrangian description of the fluid through particles moving at the fluid velocity and carrying physical properties such as mass, volume, momentum and energy. This method was originally developed for astrophysics [5] and later adapted to free surface flow [6]. One advantage of SPH over traditional grid-based methods in simulating multi-phase flow is the natural description of the gas/liquid interface by the arrangement of gas and liquid particles, so that no reconstruction algorithm is required.

In the field of air-assisted liquid atomization, the gas/liquid momentum transfer is the driving phenomenon so that both phases must be accurately resolved at their interface. The large density and viscosity ratio of fluids typically involved in air-assisted liquid atomization brings an additional challenge in terms of stability and accuracy. This particular context constitutes an original use of the SPH method that was initiated by Höfler *et al.* [7]. Takashima *et al.* [8] assessed the SPH method for a liquid jet breakup in the Rayleigh regime. Braun and coworkers applied the SPH method to a droplet in a sheared flow [9] and to a generic planar prefilming airblast atomizer [10] where it was shown that the method retrieves the proper behavior of the liquid fragmentation. Dauch *et al.* [11] investigated a realistic annular prefilming airblast atomizer and demonstrated the suitability of the SPH method in complex industrial configuration. Finally, Chaussonnet *et al.* [12] investigated the air-assisted atomization of a viscous liquid at atmospheric pressure in a geometry similar to the one of the present study.

In the field of non-newtonian SPH, Shao *et al.* [13] investigated the behavior of mud in the dam break configuration, Hosseini *et al.* [14] applied different rheological models in several simple test-cases, and Shamsoddini *et al.* [15] simulated the industrial configuration of an active micro-mixer with a power-law fluid. Finally Qiang *et al.* [16] studied the breakup of two impinging power-law liquid jets. Note that in this case, the gas phase has a negligible influence on the breakup process. For an extensive review of the capability of SPH in a broad range of industrial applications, the reader is referred to [17].

The experiment is presented in a first part, followed by a description of the numerical model. The simulation results are compared to the experiment in the final part.

## EXPERIMENT

Sänger and coworkers studied the fragmentation mechanism of a viscous fluid in a *twin-fluid external mixing atomizer* at atmospheric pressure (ATMO test-rig) [2] and at high pressure (PAT test-rig) [3]. The nozzle is depicted in Fig. 1 and consists of an axial liquid jet sheared by a co-flowing high speed gas stream discharging into a quiescent cavity.

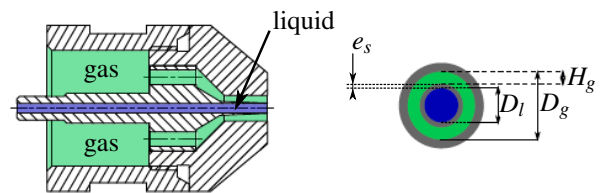


**FIGURE 1:** Schematics of external mixing twin fluid atomizer, side view (*left*) and front view (*right*).

The liquid diameter  $D_l$ , the gas height  $H_g$ , the separator thickness  $e_s$  and the gas diameter  $D_g$  are equal to 2, 1.6, 0.1 and 5.4 mm, respectively. Two types of liquid, L1 and L2, were simulated. The former is a Newtonian liquid composed of a mix of water and glycerol, while the latter is a non-Newtonian solution obtained with carboxymethyl cellulose (CMC) solution that shows an apparent viscosity comparable to L1 in the investigated operating conditions [4]. Their characteristics are recalled in Table 1. The viscosity of liquid L2 is modeled with the Cross model

$$\mu = \frac{\mu_0 - \mu_\infty}{1 + (\tau \dot{\gamma})^m} + \mu_\infty \quad (1)$$

where  $\eta_0$  and  $\eta_\infty$  are effective dynamic viscosities at zero and infinite shear rate, respectively. Their values were measured with a Searle type rheometer where the shear rate  $\dot{\gamma}$  was varied from 1 to  $4000 \text{ s}^{-1}$ , and are exhibited in Table 1. The constant  $\tau$  represents a characteristic time scale and  $m$  is an additional constant of the fluid. They were calculated to 0.630 and  $6.02 \times 10^{-3}$ , respectively. Figure 2 depicts the excellent agreement between measurements and the Cross model in the considered range of shear rate. Nevertheless as seen later, the shear rate in the liquid can reach values up to  $10^6 \text{ s}^{-1}$ , and the liquid viscosity was not measured to such high shear rates.

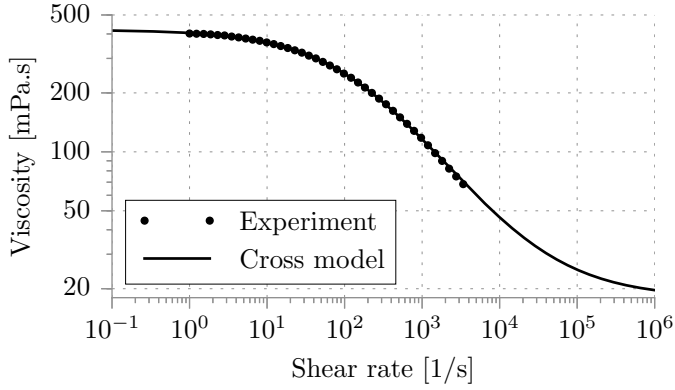


**FIGURE 2:** Effective viscosity versus the shear rate.

**TABLE 1:** Experimental parameters and test conditions.

Parameter	Variable	Unit	Liq. L1	Liq. L2
Density	$\rho$	$\text{kg m}^{-3}$	1233	1006
Dyn. viscosity	$\mu$	mPa.s	200	$\approx 151^*$
Viscosity lim.	$\mu_0, \mu_\infty$	mPa.s	—	420, 18
Surface tension	$\sigma$	$\text{mN m}^{-1}$	63.6	68.9

\* apparent viscosity in the investigated conditions.

The nondimensional numbers that characterize this configuration are:

$$\text{Re} = \frac{\rho D_h U}{\mu}, \text{We} = \frac{\rho_g D_l U_{rel}^2}{\sigma}, \text{GLR} = \frac{\dot{m}_g}{\dot{m}_l}, \text{M} = \frac{\rho_g U_g^2}{\rho_l U_l^2} \quad (2)$$

Equations (2) shows, in order of appearance: the Reynolds number where  $D_h$  is the hydraulic diameter equal to  $D_l$  for the liquid and  $2H_g$  for the gas, the Weber number where  $U_{rel}$  is the liquid/gas relative velocity, the Gas-To-Liquid ratio, and the momentum flux ratio, respectively. The Ohnesorge number defined as  $\mu_l / \sqrt{\sigma \rho_l D_l}$  is 0.50 for L1 and varies between 0.048 and 0.62 for L2.

The liquid disintegration was recorded with a high-speed camera. It was observed in the ATMO rig that the jet undergoes different types of primary instability (pulsating and flapping modes) depending on the liquid viscosity at constant GLR as illustrated in Fig. 3a) and b), leading to two different spray characteristics. It was also found that the breakup regime changes from a *membrane* type to a *fiber* type breakup when the pressure increases at constant gas velocity (Fig. 3c and d).

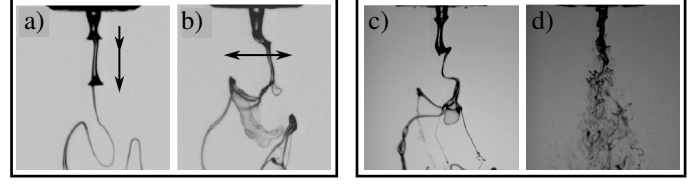


**FIGURE 3:** Primary instability: a) pulsating ( $\mu_l = 200$  mPa.s) and b) flapping ( $\mu_l = 300$  mPa.s), from [2]. Breakup regime: c) membrane type ( $p = 1$  bar abs.) and d) fiber type ( $p = 7$  bar abs.), from [3].

## NUMERICAL MODEL

The starting point of the SPH discretization is the convolution of a field  $f(\mathbf{r})$  by a Dirac function  $\delta(\mathbf{r})$ :

$$f(\mathbf{r}) = \int f(\mathbf{r}') \delta(\mathbf{r} - \mathbf{r}') d\mathbf{r}' \quad (3)$$

In a first step called the kernel approximation, the Dirac function is replaced by a smooth interpolation function  $W(\mathbf{r} - \mathbf{r}', h)$  called the kernel and depicted in Fig. 4 (top). This function is defined on a compact support, the so-called *sphere of influence* that depends on the *smoothing length*  $h$ , and must fulfill mathematical properties such as the unity integral ( $\int W(\mathbf{r} - \mathbf{r}', h) d\mathbf{r}' = 1$ ) and the convergence to  $\delta$  when  $h \rightarrow 0$ . The kernel approximation is applied to discrete particles by a quadrature called the particle approximation. The function  $f$  is thus expressed at the particle location  $\mathbf{r}_a$  by:

$$f(\mathbf{r}_a) = \sum_{b \in \Omega} V_b f(\mathbf{r}_b) W(\mathbf{r}_b - \mathbf{r}_a, h) \quad (4)$$

where  $V_b$  is the volume of particle  $b$ . The index  $b$  refers to neighbour particles located in  $\Omega$ , the sphere of influence of the particle  $a$ , as illustrated in Fig. 4 (bottom). The kernel is chosen here as a quintic spline and  $h = \Delta x$  where  $\Delta x$  is the mean particle spacing, and the radius of  $\Omega$  is  $R = 3\Delta x$ . For the sake of clarity, in the following,  $f(\mathbf{r}_a)$ ,  $f(\mathbf{r}_b)$  and  $W(\mathbf{r}_b - \mathbf{r}_a, h)$  are shortened to  $f_a$ ,  $f_b$  and  $W_{ab}$ , respectively.

The differential operators needed to evaluate the contact forces are computed with the gradient of the kernel. The gradient  $\nabla f_a$  [18] and the Laplacian  $\Delta f_a$  [19] are expressed as:

$$\nabla f_a = \sum_{b \in \Omega} V_b (f_b + f_a) \nabla W_{ab} \quad (5a)$$

$$\Delta f_a = 2 \sum_{b \in \Omega} V_b (f_b - f_a) \frac{\partial W_{ab}}{\partial r} \quad (5b)$$

The Navier-Stokes equations of an isothermal multiphase flow are subsequently turned to a SPH form, and applied to both the

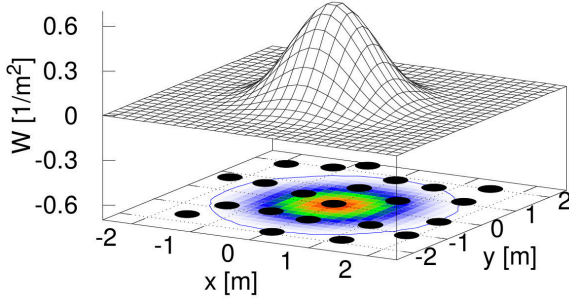


**FIGURE 4:** Top part: surface of a 2D kernel. Bottom part: particle distribution superimposed with the kernel value and illustration of the sphere of influence.

liquid and the gas phase. The continuity equation is solved algebraically by computing the particle volume and density:

$$V_a = 1 / \sum_{b \in \Omega} W_{ab} \quad \text{and} \quad \rho_a = m_a / V_a \quad (6)$$

where  $m_a$  is the constant mass of particle  $a$ . Equations (6) exactly conserve mass and as it relies only on the particle volume, the density expression avoids numerical diffusion of density near the liquid/gas interface [20]. The momentum equation is given by

$$\rho_a \left. \frac{d\mathbf{u}}{dt} \right|_a = \mathbf{f}_{a,p} + \mathbf{f}_{a,v} + \mathbf{f}_{a,st} \quad (7)$$

where  $\mathbf{u}$  is the particle velocity and the terms  $\mathbf{f}_{p,a}$ ,  $\mathbf{f}_{v,a}$  and  $\mathbf{f}_{st,a}$  are the forces due to pressure, viscosity and surface tension, respectively. They yield:

$$\mathbf{f}_{a,p} = - \sum_{b \in \Omega} V_b (p_b + p_a) \nabla W_{ab} \quad (8a)$$

$$\mathbf{f}_{a,v} = K \sum_{b \in \Omega} V_b \bar{\mu} \frac{\mathbf{u}_{ab} \cdot \mathbf{r}_{ab}}{r_{ab}^2 + \eta^2} \nabla W_{ab} \quad (8b)$$

$$\mathbf{f}_{a,st} = - \sigma_a \kappa \delta_\Sigma \mathbf{n} \quad (8c)$$

Equations 8a and 8b are the SPH expressions of the pressure gradient and velocity Laplacian. Additionally, Eq. 8b introduces the prefactor  $K$  equal to 8 in 2D [21], the inter-particle viscosity  $\bar{\mu}$  is derived from a density-based average explained later. Equation 8b also involves the scalar product of velocity difference  $\mathbf{u}_{ab} = \mathbf{u}_a - \mathbf{u}_b$  by the inter-particle distance vector  $\mathbf{r}_{ab} = \mathbf{r}_a - \mathbf{r}_b$ . The term  $\eta = 0.1 h$  avoids the singularity when  $r_{ab}^2 = 0$ . In the surface tension force (Eq. 8c),  $\sigma_a$  is the surface tension coefficient at particle  $a$  and  $\kappa$  is the interface curvature. The terms  $\mathbf{n}$  and  $\delta_\Sigma$  are the interface normal and the surface-delta function, respectively [22].

To close the system, the pressure is expressed through a Tait equation of state that depends on the particle density only:

$$p_a = \frac{\rho_0 c^2}{\gamma} \left[ \left( \frac{\rho_a}{\rho_0} \right)^\gamma - 1 \right] + p_{back} \quad (9)$$

where  $\rho_0$  is the nominal particle density,  $\gamma$  is the polytropic ratio and  $p_{back}$  is the background pressure. The term  $c$  in Eq. (9) is the artificial speed of sound and must be chosen to verify  $c \geq 10 u_{max}$  in order to fulfill the weakly compressible condition by ensuring that density variation is lower than 1% [23], the final purpose being to increase the time step through the CFL condition. The inter-particle viscosity  $\bar{\mu}$  in Eq. 8b yields:

$$\bar{\mu} = 2 \frac{\rho_a \rho_b}{\rho_a + \rho_b} \frac{\nu_a + \nu_b}{2} \quad (10)$$

where  $\nu = \mu/\rho$  is the kinematic viscosity. Equation 10 can be seen as a blending function for the viscosity that favors the liquid of lower density in the interface zone. In the case of a non-Newtonian fluid, the viscosity  $\mu_a$  of particle  $a$  is expressed by Eq. 1 where the shear rate is given by  $\dot{\gamma} = \sqrt{2 \text{tr}(\mathbb{D}^2)}$ ,  $\mathbb{D}$  being the trace-free shear rate tensor which represents the fluid deformation with no change of volume:

$$\mathbb{D} = \frac{1}{2} (\mathbb{U} + {}^t\mathbb{U}) - \frac{\text{tr}(\mathbb{U})}{N} \mathbb{I} \quad (11)$$

where  $\mathbb{U}$  is the velocity gradient and  $N$  the number of dimension. In 2D,  $\dot{\gamma}$  is expressed as:

$$\dot{\gamma} = \sqrt{\left( \frac{\partial u}{\partial x} - \frac{\partial v}{\partial y} \right)^2 + \left( \frac{\partial u}{\partial y} + \frac{\partial v}{\partial x} \right)^2} \quad (12)$$

and the velocity gradient  $\mathbb{U}$  is approximated with the SPH operator:

$$\mathbb{U} = \nabla \otimes \mathbf{u} = \sum_{b \in \Omega} V_b (\mathbf{u}_b - \mathbf{u}_a) \otimes \nabla W_{ab} \quad (13)$$

As the simulations conducted in this paper are 2D, three modifications are added to the numerical method to represent the 3D effects of the experiment. First, in order to take into account the curvature of the round jet interface, an artificial surface tension force

$$\mathbf{f}_{a,curv} = -\epsilon_x \epsilon_y \frac{\sigma_a}{|y|} \delta_\Sigma \mathbf{n} \quad \text{with} \quad \begin{cases} \epsilon_y = 1 - \exp\left(-\frac{y^2}{h^2}\right) \\ \epsilon_x = \left(1 - \frac{x}{L_c}\right)^{0.2} \end{cases} \quad (14)$$

is added to the momentum equation. The term  $y$  is the radial coordinate and  $\varepsilon_y$  a damping function to avoid the singularity at  $y = 0$ . The function  $\varepsilon_x$  ensures that far from the nozzle, the artificial surface tension force is zero. It is defined between 0 and the length of the potential core  $L_c$ , expressed as  $6D_l/\sqrt{M}$  by [24]. The second modification is to adapt the vector operators expressed in a cylindrical system to their Cartesian expressions, in order to take into account the divergence of the fields with  $y$  ( $r$  in the cylindrical system). The comparison between Cartesian  $(x,y)$  and cylindrical  $(r,z)$  coordinates shows no difference for the gradient operator whereas the Laplacian differences yield, for the velocity:

$$\Delta_{CYL}(U_r) = \Delta_{CART}(U_y) + \frac{1}{y} \frac{\partial U_y}{\partial y} - \frac{U_y}{y^2} \quad (15a)$$

$$\Delta_{CYL}(U_z) = \Delta_{CART}(U_x) + \frac{1}{y} \frac{\partial U_x}{\partial y} \quad (15b)$$

The Laplacian operator, used for viscosity, is thus modified according to Eqs (15a) and (15b), the additional terms being also multiplied by  $\varepsilon_y$  (Eq. 14) to avoid singularity at  $y = 0$ . Physically, this modification aims to render the difference of the shearing surface between the inner and the outer radius of an infinitesimal element.

The third modification is to take the mass conservation into account in the radial velocity. For a constant mass flow rate along the radial coordinate, the mass conservation imposes that the velocity decreases along the radial axis. By expressing this condition in a differential form between  $y$  and  $y + dy$ , neglecting the density change over  $dy$  and second order terms, the radial velocity yields:

$$U_r^{CYL}|_{r+dr} = U_y^{CART}|_{y+dy} \left(1 - \frac{dy}{y}\right) \quad (16)$$

These corrections are particularly significant at small radius (terms in "1/y") but becomes negligible in outer regions. Note that the modifications do not aim to model an axisymmetric domain but only the center slice of an axial configuration, so that it is not necessary to modify the computation of density.

## NUMERICAL SETUP

The numerical domain depicted in Fig. 5 is composed of the inlet ducts and the cavity (length of 40 mm) where atomization takes place. The length of inlet ducts are six jet diameters for the gas and one diameter for the liquid, and the inlet velocity profiles are turbulent and laminar, respectively. A no-slip boundary condition is imposed at the walls of the inlets duct and the nozzle (all walls included in the dashed rectangle in Fig. 5 left). In order to reproduce the entrainment rate  $\dot{Q}_e$  induced by the gaseous

jets in the experiment, the cavity is fed with a coaxial gas stream with a bulk velocity  $\bar{u}_e = 10$  m/s over a slit of height  $H_e$  of 8 mm (green lines in Fig. 5 left), which guarantees a correct  $\dot{Q}_e$  up to an arbitrary distance of 10 mm according to the free jet entrainment law. On the sides of the cavity, the velocity is mainly axial due to the entrained flow, so that the use of an outflow boundary condition would generate a strong numerical noise. Therefore, the sides are set to slipping walls and they open with an angle larger than the free jet opening angle (semi-angle of  $15^\circ$ ). The outlet is set to a constant pressure equal to 1, 7 or 11 bar. The chamfer of the nozzle is added to improve the interaction between the outer recirculation zone and the nozzle itself. With a particle size  $\Delta x$

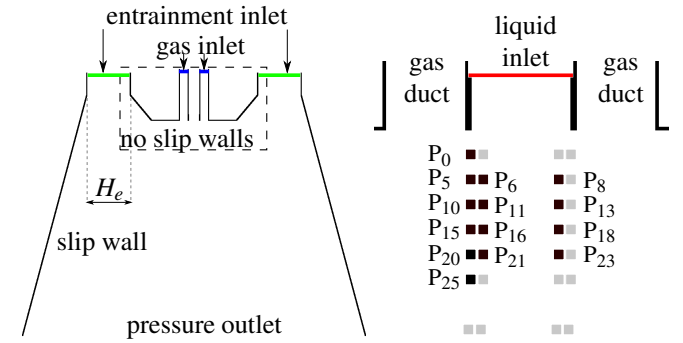


**FIGURE 5:** Sketch of the numerical domains. Left: global view. Right: closeup of the nozzle exit superimposed with all probes location (grey), the black symbols indicates the probes investigated in the following.

of 10 and 20  $\mu\text{m}$ , the numerical domain is contains 23.3 and 5.83 millions of particles, respectively. The initial solution consists of a cavity filled with SPH particles of gas type. The calculations are run in parallel on up to 2560 CPU, during a physical time of 45 ms with a time step  $\Delta t$  of 20 ns. This results in 67 convective times that ensures an acceptable statistic convergence.

## RESULTS AND DISCUSSION

The investigated cases are summarized in Table 2. First, simulations with the Newtonian liquid L1 and different pressures are conducted (cases A, B and C) to check that the breakup regime (membrane and fiber) is well recovered, then a simulation with the non-Newtonian liquid L2 is run at 1 bar (case D). Finally the atomization of liquid L2 is investigated at high pressure with case E for two different resolutions.

### Newtonian liquid at different ambient pressures

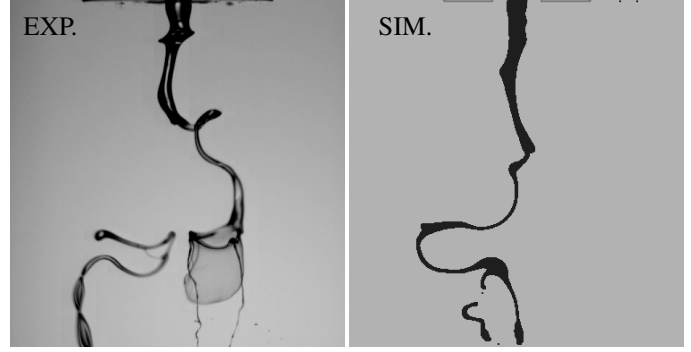
Cases A, B and C are qualitatively compared to the experiment in Fig. 6, which depicts snapshots of the liquid phase. The

**TABLE 2:** Test-case matrix.

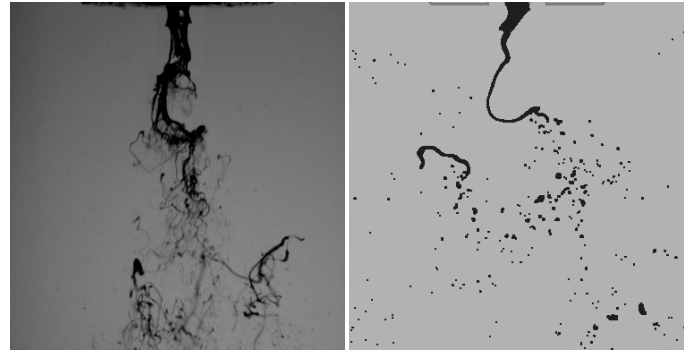
Param.	Unit	A	B	C	D	E
$p$	bar	1	7	11	1	11
$\rho_g$	$\text{kg m}^{-3}$	1.20	8.43	13.25	1.20	13.25
$U_g$	m/s	58.3	58.3	58.3	72.8	58.3
Liq. type	–	L1	L1	L1	L2	L2
$\Delta x$	$\mu\text{m}$	20	20	20	20	10/20
$\text{Re}_g$	$1 \times 10^3$	17.0	119	187	21.2	187
We	–	125	874	1375	181	1269
GLR	–	0.4	2.8	4.4	0.6	5.5
$M$	–	4.5	31	49	8.2	62

behavior of the liquid jet is qualitatively well captured by the simulation for each case. At 1 bar, the jet disrupts into a single ligament that sometimes forms a membrane (membrane-type regime). In the numerical simulation, the characteristic scale as well as the curvature of the ligament are similar to the experiment. However the space discretization is too coarse to capture the membrane. At 7 bar, the experiment shows a fiber-type regime, characterized by a liquid jet peeled-off in small scale fibers, and a shorter intact length. The simulation is too coarse to predict the fibers, however it is able to capture the small scale structure, under the form of small droplets. In addition, it succeeds to predict the shorter intact length of the fiber-type regime. Case C corresponds to a pulsating mode [25] of the fiber-type regime, which exhibits local changes of volume fraction in the spray. This behavior is also observed in the simulation even though it is not easily visible on one snapshot. The comments of 7 bar also applies to 11 bar.

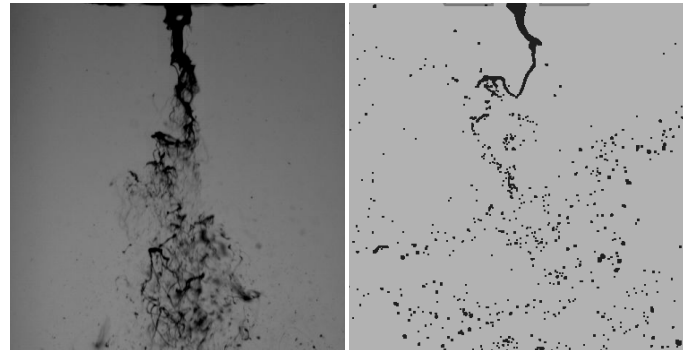
For all cases, the experiment shows that the jet undergoes a Kelvin-Helmholtz (KH) instability under the form an axisymmetric disturbance at the nozzle exit, whereas the simulation captures a KH instability that alternates on both sides of the liquid, instead of being axisymmetric. Most of the time, this difference leads to a frequency prediction, underestimated by a factor 2, compared to the experiment. In addition, the alternating KH instability results in a flapping motion whereas the experiment shows a pulsating instability. These discrepancies might originate from the inability of the 2D simulation to render the stiffness of the liquid jet, despite the 3D correcting terms, and is explained in the following. When a round jet undergoes a local deformation, due to *e.g.* an eddy, the local variation of curvature leads to a heterogeneous distribution of the capillary pressure force induced by the surface tension, as depicted in Fig. 7 (*top left*). Thus, the resultant force is oriented upwards and counteracts the source of the perturbation. When a planar liquid sheet, which corresponds to the 2D simulation, undergoes the same vertical



a) Case A,  $p = 1$  bar



b) Case B,  $p = 7$  bar



c) Case C,  $p = 11$  bar

**FIGURE 6:** Comparison of experiment/simulation on PAT test-case at 1, 7 and 11 bar.

deformation (Fig. 7 *bottom left*), the artificial force induced by the 3D correcting term (Eq. 14) is rather constant on both faces of the sheet. Therefore, the resultant force is zero and cannot counteract the source of the perturbation, so that the jet will be deflected downwards. However, the liquid/gas momentum transfer is correctly predicted and the onset frequency of the KH instability equal to the one of the round jet, but the liquid sheet

is deflected towards the opposite side of the perturbation. This leads to a flapping jet with the flapping half-time equal to the onset time of the KH instability, as illustrated in Fig. 7(right). As a result, the estimation of the KH frequency based on the liquid detection presented below leads to a frequency twice lower as it might be in a 3D case. This implies that (i) the set of 3D corrections terms is incomplete to properly retrieve a correct 3D instability and (ii) it is expected that a 3D simulation would retrieve a correct frequency estimation.

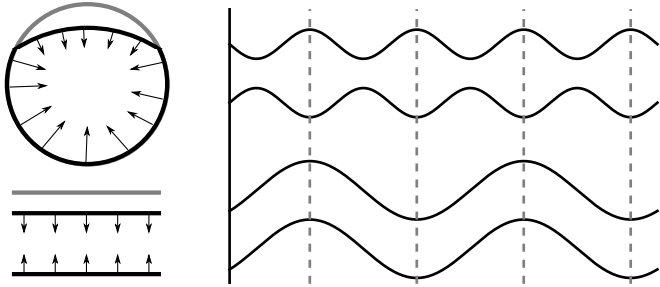


**FIGURE 7:** Left: front view of a round jet (*top*) and a flat liquid sheet (*bottom*) after a deformation, superimposed with the local forces induced by the surface tension. The original location of the interface is depicted in gray. Right: sketch of the axisymmetric Kelvin-Helmholtz instability in the (3D) experiment (*top*) and in the 2D simulation (*bottom*).

The presence of liquid was monitored in the numerical simulation on several virtual probes (Fig. 5 *right*) located at the nozzle exit close to the liquid jet interface, to capture the KH instability. A time signal  $s$  between 0 (gas) and 1 (liquid) was extracted on each probe. A Fourier Transform (FT)  $\mathcal{F}(s)$  was applied on the signal and the Cross Spectral Density (CSD) between two probes (*e.g.*  $P_0$  and  $P_5$ ) was calculated as  $CSD(f) = \mathcal{F}(s_0) \cdot \mathcal{F}^*(s_5)$  where  $*$  is the conjugate operation. The CSD allows to filter out the uncorrelated noise on the probes and keep the frequencies shared by the two probes. Furthermore, the cross-correlation of the two temporal signals was calculated to estimate the time delay  $\tau_{cc}$  between associated two probes.

Figure 8 (*top*) shows the time signal of the liquid presence recorded at probes  $P_5$  and  $P_{20}$  for Case A. The periodic pattern is representative of the KH instability at the jet surface, a roughly constant time delay is observed. The CSD between ( $P_{10}, P_{15}$ ), ( $P_{10}, P_{20}$ ) and ( $P_{10}, P_{25}$ ) are depicted in Fig. 8 (*bottom*). They show the same peaks at 170 and 251 Hz, which is lower than in the experiment where  $f = 524$  Hz. Since the frequency measured in the experiment is 524 Hz, the pulsating frequency is underestimated by a factor of two, as explained earlier. Therefore, if the simulation were predicting an axisymmetric KH instability, the frequency would be correctly predicted. Calculating the time

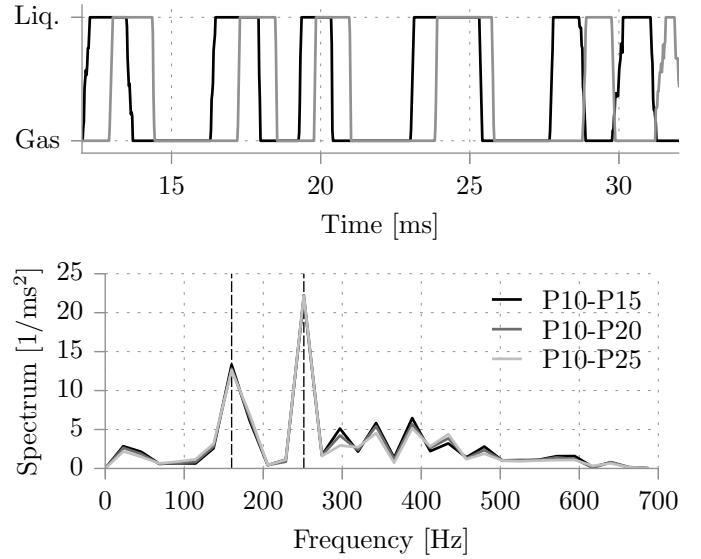


**FIGURE 8:** Time signal of liquid presence (*top*) recorded at probes  $P_{10}$  and  $P_{25}$  and the cross-spectrum magnitude (*bottom*) between different probes, for Case A.

delay  $\tau_{cc}$  from the cross-correlation of the signals leads to 283, 554, 821  $\mu$ s. Combining  $\tau_{cc}$  with the inter-probe distances  $\Delta x$  lead to a propagation velocity of 1.77, 1.80 and 1.83 m/s. The average velocity is 1.80 m/s to be compared with the Dimotakis velocity [26]  $U_D$  equal to 2.59 m/s and defined by:

$$U_D = \frac{\sqrt{\rho_l} U_l + \sqrt{\rho_g} U_g}{\sqrt{\rho_l} + \sqrt{\rho_g}} \quad (17)$$

Considering Case B, Fig. 9 (*top*) shows the time signal of  $P_0$  and  $P_{15}$ , located at the liquid jet interfaces, 0.5 and 2 mm downstream the nozzle exit, respectively. The signals show a clear periodic event with a constant time delay between the two probes. The CSD between probes spaced of  $\Delta x = 0.5, 1$  and 1.5 mm are presented in Fig. 9 (*bottom*), and show two peaks located at 755 and 1486 Hz, corresponding to the fundamental mode and its first harmonic. As for Case A, the underestimation by a factor 2 of the fundamental frequency is attributed to an alternating KH instability. The time delays  $\tau_{cc}$  from the cross-correlation of the signals leads to 131, 230, 314  $\mu$ s, which results to a propagation velocity of 3.82, 4.34 and 4.78 m/s. The average velocity is 4.31 m/s to be compared with the Dimotakis velocity  $U_D$  equal to 5.24 m/s, which is in acceptable agreement and suggests a correct momentum transfer from the gas to the liquid for Case B.

Figure 10 (*top*) shows the time signal recorded for Case C. Due to a more more turbulent flow, the gas/liquid interface is more disturbed so that the signal is distorted, but still shows periodic events. The CSD between probes spaced of  $\Delta x = 0.5, 1$  and

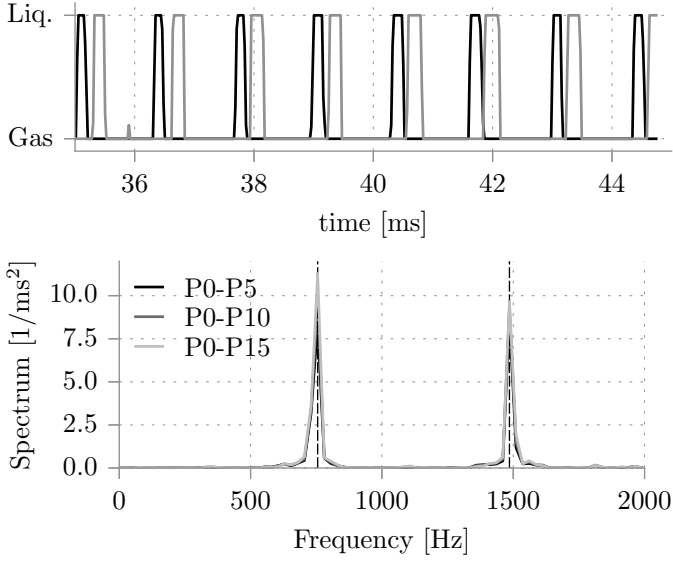


**FIGURE 9:** Time signal of liquid presence (top) recorded at probes P<sub>0</sub> and P<sub>15</sub>, and the CSD magnitude (bottom) between different probes, for Case B.

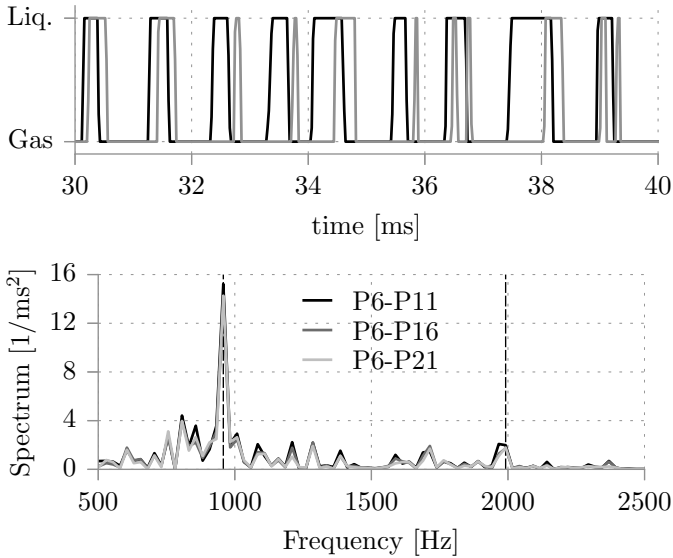


**FIGURE 10:** Time signal of liquid presence (top) recorded at probes P<sub>6</sub> and P<sub>21</sub>, and the cross-spectrum magnitude (bottom) between different probes, for Case C. Then vertical lines represent the fundamental mode and its first harmonic.

1.5 mm are presented in Fig. 10 (bottom). The fundamental frequency  $f_0$  and its first harmonic  $f_1$  are found at 958 and 1991 Hz, respectively, whereas  $f_{\text{exp}} = 2153$  Hz. The underestimation by a factor 2 of the frequency  $f_0$  is attributed to an alternating KH instability, as seen in the two previous cases. The time delays

are 73, 127 and 162  $\mu\text{s}$  and lead to a convective velocity of 6.88, 7.87 and 9.25 m/s. Their average is 8.00 m/s, which is slightly overestimating  $U_D = 6.25$  m/s. The growth of the convective velocity with  $x$  may be explained by increasing perturbations of the liquid jet surface, leading to degenerated conditions where the calculation of  $U_D$  is not valid anymore.

### Non-Newtonian liquid at 1 bar

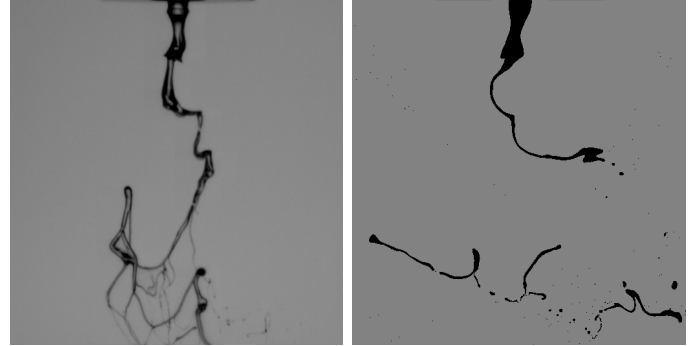


**FIGURE 11:** Comparison of experiment/simulation at 1 bar with liquid L2.

Figure 11 displays a comparative snapshot of the experiment and the simulation for Case D. The agreement is good in terms of intact length ligament characteristic length. However the experiment shows a pulsating mode whereas the simulation predicts a flapping behavior. In order to highlight the influence of the non-Newtonian model, Fig. 12 depicts a closeup view of the nozzle exit, colored by the shear rate  $\dot{\gamma}$  (left) and the viscosity (right). The shear rate is large at the gas/liquid interface and minimum at the center of the jet. Moreover, it is larger further downstream as the liquid jet becomes thinner because its inertia decreases so that it is more influenced by the aerodynamic stresses. The viscosity follows this influence, with particularly low values at the gas/liquid interface, and at the end of the intact length. Because of the shear-thinning behavior of the liquid, an amplification loop occurs at the jet interface: due to the high shearing induced by the aerodynamics stresses, the liquid viscosity decreases, offering less shear resistance to the gas which, in turn, accelerates the liquid deformation *i.e.* the shear rate. Note that this effect is limited to the outer part of the liquid jet, and the core part is less influenced by the non-Newtonian effect, due to a moderate shearing.

The cross-spectra between pairs of probes (P<sub>0</sub>,P<sub>5</sub>), (P<sub>0</sub>,P<sub>10</sub>) and (P<sub>0</sub>,P<sub>15</sub>) is shown in Fig. 13. Many peaks of the same value are observed, so that the fundamental mode is not obvious. The time delays  $\tau_{cc}$  are 290, 534 and 791  $\mu\text{s}$  and lead to a convection velocities of 1.72, 1.87 and 1.97 m/s while  $U_D = 3.28$  m/s.

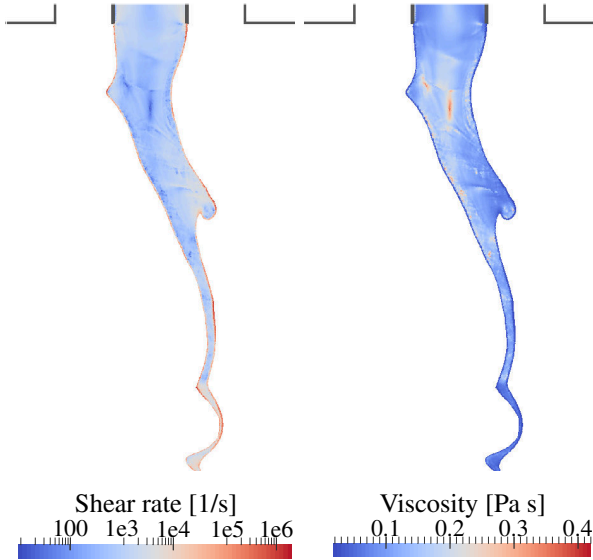


**FIGURE 12:** Closeup view of the nozzle exit. Left: shear rate. Right: viscosity.

This deviation may originate from a significant effect of the non-Newtonian aspect of the liquid on the Dimotakis velocity, even though the viscosity does not appear in the expression of  $U_D$ .

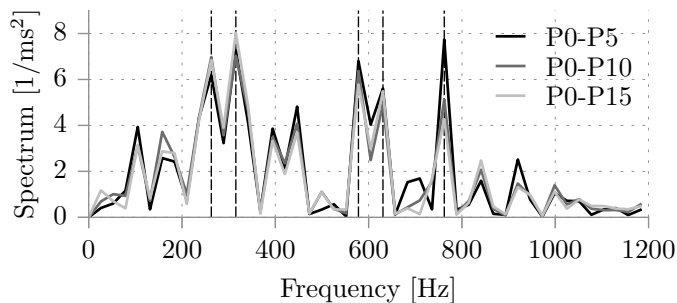


**FIGURE 13:** Fourier transform of liquid presence signal for L2 at 1 bar.

### Non-Newtonian liquid at 11 bar

The atomization of non-Newtonian liquid L2 was simulated at an ambient pressure of 11 bar, with a space discretization of  $10\ \mu\text{m}$ . A snapshot comparison between L1 and L2 is displayed in Fig. 14. The intact length is similar in both cases because of the moderate liquid shear rate in the core of the jet. In Case E, the characteristic length of the ligaments torn from the jet is significantly lower than Case C and many more smaller droplets are created. In order to be sure that this trend does not originate from

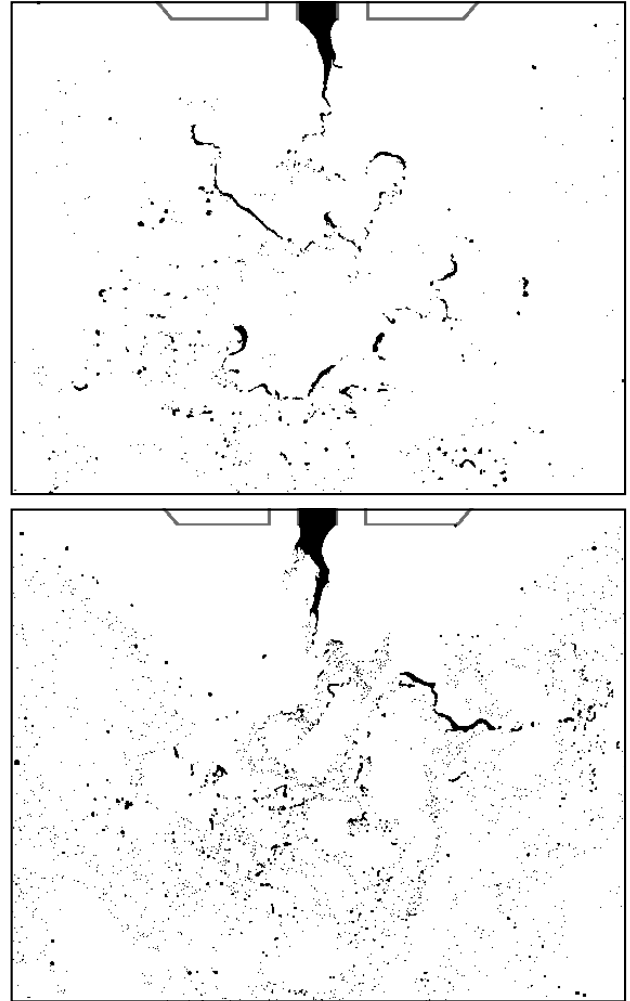


**FIGURE 14:** Snapshot of Case C (top) and Case E (bottom).

the finer space discretization, Case E was also simulated with  $\Delta x = 20\ \mu\text{m}$  and the structures are also significantly lower than Case C. This suggests that the atomization of a non-Newtonian liquid at high pressure also leads to a fiber-type regime, with a larger number of fibers of smaller length scale compared to with a Newtonian liquid of the same apparent viscosity. This behavior was also experimentally observed by Sanger *et al.* [4] at atmospheric pressure, where they highlighted the favorable influence of the shear-thinning property in the fragmentation of non-Newtonian liquids. Note that the spacial distribution of the liquid phase is more homogeneous in Case E due the smaller fibers. Finally, the larger number of droplets visible in the top corners of Fig. 14 *bottom* in comparison to Case C is attributed to the strong recirculation zone that drags the smaller particles.

The CSD between the pairs  $(P_8, P_{13})$ ,  $(P_8, P_{18})$  and  $(P_8, P_{23})$  are displayed in Fig.15, and peaks at 1252 and 1388 Hz are observed. If the same phenomenon of alternating KH instability in-

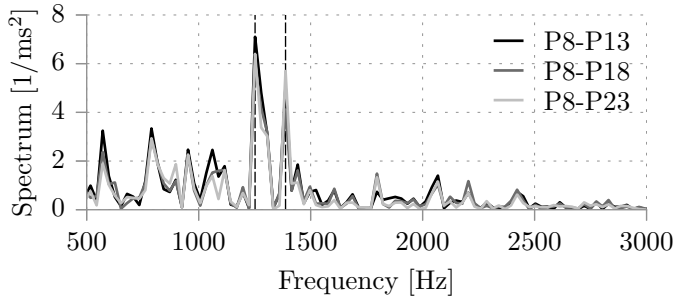


**FIGURE 15:** Fourier transform of liquid presence signal for L2 at 11 bar with  $\Delta x = 10 \mu\text{m}$ .

stead of axisymmetric KH instability is assumed in this case, then the pulsating frequency is estimated between 2500 and 2800 Hz. The time delays  $\tau_{cc}$  are 31, 73 and 108  $\mu\text{s}$ . The convective velocities extracted from  $\tau_{cc}$  are 15.9, 13.7 and 13.9 m/s whereas the Dimotakis velocity is 6.8 m/s. The most probable reason for this large deviation is that the jet is already very disturbed at 1 mm downstream the nozzle exit, the conditions to derive the Dimotakis velocity are not met. It is to be noted that the spectrum of Case E is similar to the one of Case C (Fig. 10), with a shift towards higher frequencies.

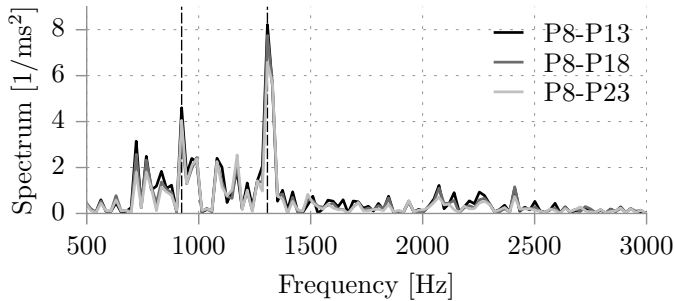


**FIGURE 16:** Fourier transform of liquid presence signal for L2 at 11 bar with  $\Delta x = 20 \mu\text{m}$ .

The CSD for Case E with  $\Delta x = 20 \mu\text{m}$  is displayed in Fig. 16. The spectrum looks similar as for Case E with  $\Delta x = 10 \mu\text{m}$ , with a noisy spectrum up to  $f \approx 1200 \text{ Hz}$ . A clear peak is found at  $f \approx 1307 \text{ Hz}$ , compared to 1252 Hz for  $\Delta x = 10 \mu\text{m}$ . This good agreement shows that  $\Delta x = 20 \mu\text{m}$  is a sufficient resolution to capture the liquid jet dynamics in these operating conditions.

A time and radial average of the liquid viscosity for Case D and Case E ( $\Delta x = 10$  and  $20 \mu\text{m}$ ) is plotted versus the axial coordinate in Fig. 17. The  $x$ -extents of the curves were limited to an arbitrary length representative of jet length. It shows that at atmospheric pressure, the mean viscosity starts at its lowest value, then reaches a peak at  $x \approx 1.5 \text{ mm}$  and decreases smoothly to a

plateau at  $\approx 110 \text{ mPa}\cdot\text{s}$ . The viscosity then is averaged between  $x = 0$  and 6 mm as done in [4] where the apparent viscosity is evaluated from the frequency of viscosity dependent KH instabilities, employing high-speed visualizations. This leads to an average viscosity of 122 mPa $\cdot$ s in the simulation, compared to an average viscosity of 151 mPa $\cdot$ s in the experiment, which is in acceptable agreement. For the two Cases E, the mean viscosity reaches its largest value directly at the nozzle exit, and continuously decreases. This particular behavior is explained by the fact that a larger air pressure increases globally the liquid entrainment, so that the jet is stretched into the cavity, leading to a substantial decrease of its diameter. This generates a recirculation zone at the nozzle exit, *e.g.* visible in Fig. 14, where the lower gas velocity induces a lower shear rate, *i.e.* a larger viscosity. In addition, the matching of the curves of Case E for  $\Delta x = 10$  and  $20 \mu\text{m}$  constitutes another formal proof of mesh convergence, implying that  $\Delta x = 20 \mu\text{m}$  is a sufficient resolution to capture the influence of the flow field on the rheological behavior of the liquid.

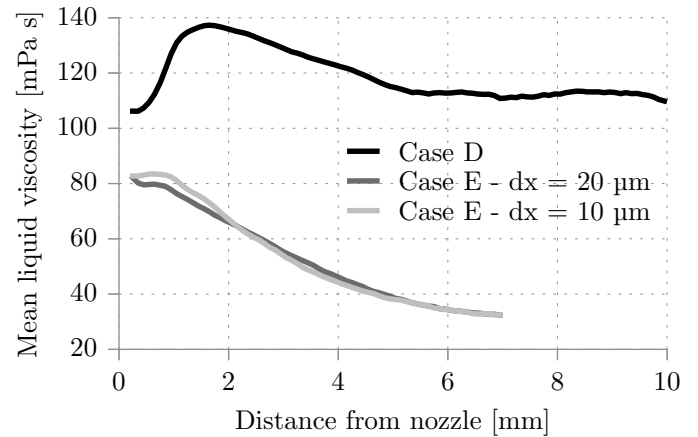


**FIGURE 17:** Time and radially average viscosity versus the axial coordinate.

Finally, a particular phenomenon is observed in Case E and illustrated in Fig. 18. Due to the deviation of the liquid jet to right, a recirculation zone appears in the wake of the nozzle, on the left of the jet. This recirculation zone rotates counterclockwise and therefore shears the liquid jet in the opposite direction of the global flow (*i.e.* from bottom to top in Fig. 18) and leads to a KH pattern moving upstream the liquid jet on one side, while the KH instability is convected downstream on the other side. This phenomenon is dramatically enhanced by the shear-thinning behavior of the liquid, as previously mentioned, an leads to an gas/liquid interaction more complex than in the case of a Newtonian fluid. As there is no experimental data for Case E yet, this phenomenon needs further validation.

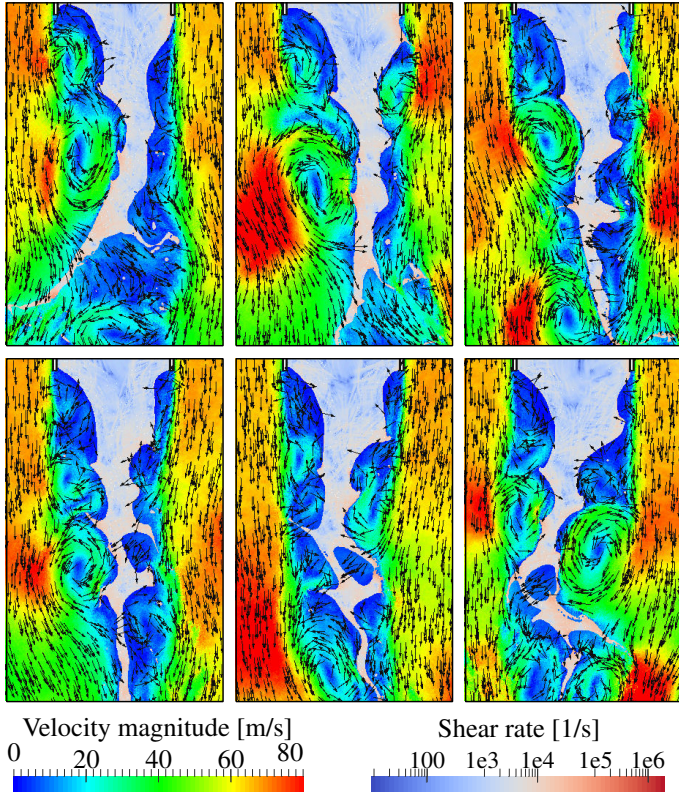


**FIGURE 18:** Time series ( $\Delta t = 100 \mu\text{s}$ ) of the breakup phenomenon zoomed in the nozzle exit region for Case E ( $\Delta x = 10 \mu\text{m}$ ). The sequence is ordered from left to right then from top to bottom.

**TABLE 3:** Comparison of measured/computed frequencies.

Frequency [Hz]	A	B	C	D	E
Simulation	251	755	958	–	$\approx 1320$
Simulation corrected	502	1486	1991	–	$\approx 2640$
Experiment	524	1479	2153	768	–
Deviation [%]	-52	-49	-56	–	–
Deviation corrected [%]	-4.2	0.47	-7.5	–	–

Table 3 summarizes the frequencies measured in the experiments and predicted by the simulations, with and without considering the factor 2. In the simulation of Newtonian liquid, taking the factor 2 into account leads to an acceptable agreement for all cases. The use of non-Newtonian liquid at 1 bar leads to a CSD too noisy to determine the fundamental mode.

## CONCLUSION

The numerical simulation of a twin fluid atomizer with SPH method showed that the simplified 2D approach does not correctly predict the mode of instability (pulsating/flapping), despite the addition of 3D correction terms. However, the numerical simulation exhibited a good qualitative agreement concerning the breakup regime (membrane or fiber-type). In addition, the dynamics and the characteristic length of the ligaments are correctly predicted, which is promising with regards to the prediction of the drop size distribution. The frequency of the Kelvin-Helmholtz instability shows a deviation of  $\approx 50\%$  due to an side-alternating onset of this instability. When this anomaly is taken into account, the introduction of a factor 2 leads to an acceptable frequency prediction, for Newtonian liquids. In the case of a non-Newtonian fluid at atmospheric pressure, the mean viscosity is in acceptable agreement with the experience, which partially validates the applicability of the SPH method in simulating the air-assisted atomization of non-Newtonian liquids. It was also shown via a mesh convergence study that an inter-particle distance of  $20 \mu\text{m}$  is sufficient to capture (i) the liquid jet dynamics and (ii) the influence of the flow field on the rheological behavior of the liquid. Finally, the 2D SPH simulation of a shear-thinning liquid highlighted a characteristic length of fibers and ligaments lower than for a Newtonian liquid, suggesting a favorable effect of shear-thinning liquids on air-assisted atomization. The next step of the study is to conduct a three-dimensional simulation on a full geometry, which will be done by creating an initial 3D domain and using a 3D formulation of the SPH method, as done previously by Braun *et al.* [27]

## ACKNOWLEDGMENT

This work was performed on the computational resource ForHLR Phase I funded by the Ministry of Science, Research and the Arts Baden-Württemberg and DFG (“Deutsche Forschungsgemeinschaft”). The Authors like to thank the Helmholtz Association of German Research Centres (HGF) for funding.

## References

- [1] Jakobs, T., Djordjevic, N., Fleck, S., Mancini, M., Weber, R., and Kolb, T., 2012. “Gasification of high viscous slurry R&D on atomization and numerical simulation”. *Applied energy*, **93**, pp. 449–456.
- [2] Sanger, A., Jakobs, T., Djordjevic, N., and Kolb, T., 2014. “Effect of primary instability of a high viscous liquid jet on the spray quality generated by a twin-fluid atomizer”. In Proceedings of the European Conference for Liquid Atomization and Spray Systems (ILASS).
- [3] Sanger, A., Jakobs, T., Djordjevic, N., and Kolb, T., 2015. “Experimental investigation on the influence of ambient pressure on twin-fluid atomization of liquids with var-

- ious viscosities”. In Proceedings of the Triennial International Conference on Liquid Atomization and Spray System (ILASS).
- [4] Sanger, A., Jakobs, T., and Kolb, T., 2016. “Using primary instability analysis for determination of apparent liquid viscosity at jet breakup atomizing non-Newtonian fluids”. In Proceedings of the European Conference for Liquid Atomization and Spray Systems (ILASS).
- [5] Gingold, R., and Monaghan, J. J., 1977. “Smoothed particle hydrodynamics: theory and application to non-spherical stars”. *Monthly Notices of the Royal Astronomical Society*, **181**, pp. 375 – 389.
- [6] Monaghan, J. J., and Kocharyan, A., 1995. “Sph simulation of multi-phase flow”. *Computer Physics Communications*, **87**, pp. 225 – 235.
- [7] Hofler, C., Braun, S., Koch, R., and Bauer, H.-J., 2011. “Towards the numerical prediction of primary atomization using smoothed particle hydrodynamics”. In Proceedings of the European Conference on Liquid Atomization and Spray Systems (ILASS).
- [8] Takashima, T., Ito, T., Shigeta, M., Izawa, S., and Fukunishi, Y., 2012. “Simulation of liquid jet breakup process by three-dimensional incompressible SPH method”. In Proceedings of 7th International Conference on Computer Fluid Dynamics (ICCFD7), pp. 9–13.
- [9] Braun, S., Hofler, C., Koch, R., and Bauer, H.-J., 2013. “Modeling fuel injection in gas turbines using the meshless smoothed particle hydrodynamics method”. In Proceedings of ASME Turbo Expo 2013.
- [10] Braun, S., Wieth, L., Koch, R., and Bauer, H.-J., 2015. “Influence of trailing edge height on primary atomization: Numerical studies applying the smoothed particle hydrodynamics (SPH) method”. In Proceedings of the International Conference on Liquid Atomization and Spray Systems (ICLASS).
- [11] Dauch, T., Braun, S., Wieth, L., Chaussonnet, G., Keller, M., Koch, R., and Bauer, H.-J., 2016. “Computation of liquid fuel atomization and mixing by means of the SPH method: application to a jet engine fuel nozzle”. *Proceedings of ASME Turbo Expo 2016*.
- [12] Chaussonnet, G., Braun, S., Wieth, L., Koch, R., Bauer, H.-J., Sanger, A., Jakobs, T., Dordjevic, N., and Kolb, T., 2015. “SPH simulation of a twin-fluid atomizer operating with a high viscosity liquid”. In Proceedings of the International Conference on Liquid Atomization and Spray Systems (ICLASS).
- [13] Shao, S., and Lo, E. Y., 2003. “Incompressible SPH method for simulating newtonian and non-newtonian flows with a free surface”. *Advances in water resources*, **26**(7), pp. 787–800.
- [14] Hosseini, S., Manzari, M., and Hannani, S., 2007. “A fully explicit three-step SPH algorithm for simulation of non-newtonian fluid flow”. *International Journal of Numerical Methods for Heat & Fluid Flow*, **17**(7), pp. 715–735.
- [15] Shamsoddini, R., Sefid, M., and Fatehi, R., 2016. “Incompressible sph modeling and analysis of non-newtonian power-law fluids, mixing in a microchannel with an oscillating stirrer”. *Journal of Mechanical Science and Technology*, **30**(1), pp. 307–316.
- [16] Qiang, H., Han, Y., Wang, G., and Liu, H., 2013. “Numerical analysis of atomization process of liquid with power law model based on SPH method”. *Journal of Propulsion Technology*, **34**(2), pp. 240–247.
- [17] Shadloo, M., Oger, G., and Le Touze, D., 2016. “Smoothed particle hydrodynamics method for fluid flows, towards industrial applications: Motivations, current state, and challenges”. *Computers & Fluids*, **136**, pp. 11–34.
- [18] Monaghan, J. J., 2005. “Smoothed particle hydrodynamics”. *Reports on Progress in Physics*, **68**, pp. 1703 – 1759.
- [19] Cleary, P., and Monaghan, J. J., 1999. “Conduction modelling using smoothed particle hydrodynamics”. *Journal of Computational Physics*, **148**, pp. 227 – 264.
- [20] Hu, X., and Adams, N., 2006. “A multi-phase SPH method for macroscopic and mesoscopic flows”. *Journal of Computational Physics*, **213**, pp. 844 – 861.
- [21] Macia, F., Antuono, M., Gonzalez, L. M., and Colagrossi, A., 2011. “Theoretical analysis of the no-slip boundary condition enforcement in SPH methods”. *Progress of theoretical physics*, **125**(6), pp. 1091–1121.
- [22] Adami, S., Hu, X., and Adams, N., 2010. “A new surface-tension formulation for multi-phase SPH using a reproducing divergence approximation”. *Journal of Computational Physics*, **229**, pp. 5011 – 5021.
- [23] Monaghan, J. J., 1994. “Simulating free surface flows with SPH”. *Journal of Computational Physics*, **110**, pp. 399 – 406.
- [24] Lasheras, J., Villermaux, E., and Hopfinger, E. J., 1998. “Break-up and atomization of a round water jet by a high-speed annular air jet”. *Journal of Fluid Mechanics*, **357**, pp. 351–379.
- [25] Farago, Z., and Chigier, N., 1992. “Morphological classification of disintegration of round liquid jets in a coaxial air stream”. *Atomization and Sprays*, **2**, pp. 137–153.
- [26] Dimotakis, P. E., 1986. “Two-dimensional shear-layer entrainment”. *AIAA journal*, **24**(11), pp. 1791–1796.
- [27] Braun, S., Wieth, L., Dauch, T., Keller, M., Chaussonnet, G., Klatt, J.-N., Hofler, C., Koch, R., and Bauer, H.-J., 2016. “HPC predictions of primary atomization with SPH: Challenges and lessons learned”. In 11th International SPHERIC Workshop.